

60 GHz Wireless Link Within Metal Enclosures: Channel Measurements and System Analysis

Seyran Khademi, *Student Member, IEEE*, Sundeep Prabhakar Chepuri, *Student Member, IEEE*, Zoubir Irahhtauten, *Member, IEEE*, Gerard J. M. Janssen, *Member, IEEE*, and Alle-Jan van der Veen, *Fellow, IEEE*

Abstract—Wireless channel measurement results for 60 GHz within a closed metal cabinet are provided. A metal cabinet is chosen to emulate the environment within a mechatronic system, which have metal enclosures in general. A frequency domain sounding technique is used to measure the wireless channel for different volumes of the metal enclosure, considering both line-of-sight (LOS) and non-line-of-sight (NLOS) scenarios. Large-scale and small-scale characteristics of the wireless channel are extracted in order to build a comprehensive channel model. In contrast to conventional indoor channels at 60 GHz, the channel in the metal enclosure is highly reflective resulting in a rich scattering environment with a significantly large root-mean-square (RMS) delay spread. Based on the obtained measurement results, the bit error rate (BER) performance is evaluated for a wideband orthogonal frequency division multiplexing (OFDM) system.

Index Terms—channel characterization and modeling, frequency domain sounding, 60 GHz measurements, orthogonal frequency division multiplexing (OFDM), root-mean-square (RMS) delay spread.

I. INTRODUCTION

Advances in wireless communications have resulted in an ever-increasing desire and demand for high-rate wireless data transfer not only for unlimited access to information and entertainment, but also for industrial usage and sensor network applications. Current wireless technology does not meet the data rates offered by wired standards like gigabit Ethernet. Recently, the unlicensed multi-GHz spectrum available around 60 GHz has gained a lot of interest, as it has the ability to support short-range high data rates in the order of Gbps [1], [2], [3].

In this paper, we consider high-rate short-range wireless communication for mechatronic systems. The demand for high data rates (peak data rate up to a few tens of Gbps) comes from a substantial number of high rate sensors and actuators, but also from a very tight control loop in which little time is allocated for the actual communications. Application areas include communication within automobiles, satellites, aircrafts or industrial machineries. These environments with metal enclosures are highly reflective, and the resulting “long” wireless channels make wireless communications very challenging.

This work was supported in part by STW under the FASTCOM project (10551).

S. Khademi, S. P. Chepuri, G. J. M. Janssen, and A.-J. van der Veen are with the Faculty of Electrical Engineering, Mathematics and Computer Science, Delft University of Technology, The Netherlands. Email: {s.khademi, s.p.chepuri, g.j.m.janssen, a.j.vanderveen}@tudelft.nl.

Z. Irahhtauten is with the Mobile Innovation Radio group, KPN, The Netherlands. Email: zoubir.irahhtauten@kpn.com

For outdoor and indoor 60 GHz wireless systems, an extensive literature exists related to channel measurements and characterization. For outdoor scenarios, the conventional 60 GHz wireless channel exhibits increased free space path-loss with up to 14 dB/km atmospheric absorption [1], [2]. This reduces the multipath effect but also makes non-line-of-sight (NLOS) communication more difficult [4]. For indoor scenarios, [5] studied the characteristics of 60 GHz channels both in space and time for short-range broad-band wireless system design. The channel multipath structure is provided based on angle of arrival (AOA) and time of arrival (TOA) components which is helpful for incorporation in spatial signal processing algorithms. Further, [6] focuses on the small-scale nature of the channel in different indoor environments. The task group TG3c¹ produced a channel modeling document [3] reporting large-scale and small-scale channel parameters for a variety of indoor environments related to WPAN systems. Another comprehensive survey on 60 GHz indoor channel models is presented in [4]. However, to the best of our knowledge, there is no report on channel measurements and modeling within a metal enclosure, as studied in the present paper.

A. Why is the 60 GHz band interesting for mechatronic systems?

Due to spectrum scarcity, the 60 GHz band has recently gained a lot of attention. Unlike the crowded 2.4 GHz and other low frequency “free” bands, unlicensed and unoccupied spectrum is abundantly available at 60 GHz. This motivation does not directly apply to mechatronic systems within closed metal enclosures, in which transmissions do not interfere with other existing communication systems. However, several properties do make communication at 60 GHz within metal enclosures interesting, as follows:

- **Small antenna size:** Higher frequencies lead to smaller size antennas, which enables us to put more antennas in a small area, and perhaps even integrate all of them on a chip [7]. The small size of the antennas makes multiple antennas more feasible for short-range wireless communications. Recently, massive-MIMO systems have been proposed in [8] which could be a milestone in boosting the data rate in wireless systems. Such systems benefit from rich scattering environments. Thus, metal

¹The IEEE P802.15.3 working group for wireless personal area networks (WPANs) introduced a task-group, referred to as TG3c.

enclosures combined with 60 GHz technology and very-large MIMO techniques should enable high data rates comparable to wired systems [9].

- **Physical available bandwidth:** More physical bandwidth is available when we go to higher carrier frequencies. E.g., the maximum physical bandwidth that can be used at $f_c = 2.4$ GHz is limited to $2f_c = 4.8$ GHz, and the usable bandwidth is often less than this. E.g., in highly dispersive channels (like metal enclosures), the usable bandwidth is reduced due to the large number of nulls in the channel frequency response.

B. Contributions and outline

For signal processing and physical layer system design, a fair parameterized model of the propagation environment is essential. This includes the delay spread in time, the Doppler spread in frequency, a shadowing and path-loss model, etc. In this paper, a 60 GHz wideband wireless channel model based on frequency domain sounding within a metal cabinet is proposed. This was considered to emulate the environment of a mechatronic system, the main motivation for this work. We present channel measurement results and their analysis for different sizes of the metal enclosure, for both line-of-sight (LOS) and non-line-of-sight (NLOS) scenarios. A comprehensive channel model is developed to attribute both the small-scale and large-scale channel characteristics.

To understand the challenges related to high data rate wireless communications in such environments, we evaluate the bit-error-rate (BER) performance of a wideband orthogonal frequency division multiplexing (OFDM) system for the measured channels, and compare these to a conventional Rayleigh fading channel. We also provide a system design based on link budget calculations for an example high data-rate system.

The remainder of this paper is organized as follows. In Section II, we discuss the measurement set-up and explain the measurement procedure. In Section III, we provide details regarding data processing to extract parameters required for channel modeling. Based on these parameters, large-scale and small-scale channel models are presented in Sections IV and V, respectively. In Section VI, we compare the measured channel with the Saleh-Valenzuela (SV) channel model suggested for the IEEE 802.15 standard. The system analysis for a wireless link is discussed in Section VII. Final remarks are made in section VIII.

II. MEASUREMENT SET-UP AND PROCEDURE

In this section, the channel measurement procedure is explained. We also provide details on the equipment used for the measurements.

A. Frequency domain sounding technique

Channel characterization can be performed in either time domain or frequency domain [10]. In the measurements provided in this paper, a frequency domain sounding technique is used. The scattering parameters (i.e. S_{11} , S_{12} , S_{21} , S_{22}) are measured using a vector network analyzer (VNA) by

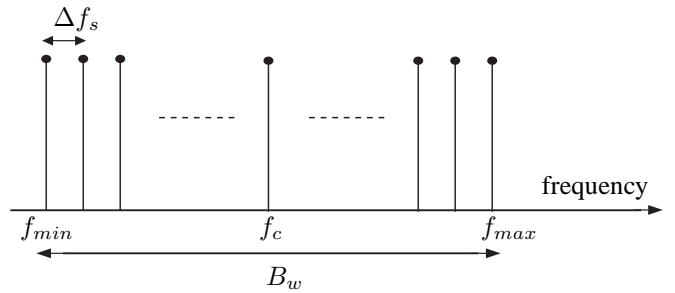


Fig. 1: Frequency domain sounding technique.

transmitting sinusoidal waves at discrete frequencies, wherein the full bandwidth of interest is sampled using an equal frequency spacing, as depicted in Fig. 1. For each of these sinusoids, the magnitude and phase of the transmitted and received signals are measured. The frequency spacing Δf_s and the scanned bandwidth B_w determine the resolution τ_{res} of the captured multipaths and the maximum measurable excess delay τ_{max} , as

$$\Delta f_s = \frac{B_w}{N_s}, \quad \tau_{max} = \frac{1}{\Delta f_s}, \quad \tau_{res} = \frac{1}{B_w}, \quad (1)$$

where N_s is the number of transmitted sinusoidal waves.

The frequency domain S_{21} parameter is generally referred to as the channel frequency response (CFR). The channel impulse response (CIR) is obtained from the measured CFR by taking the inverse fast Fourier transform (IFFT). A Hann window is applied to reduce the effect of side lobes.

B. Measurement set-up

The measurement bandwidth is set to $B_w = 5$ GHz, and the channel is sampled from 57 GHz to 62 GHz at $N_s = 12001$ frequency points. This results in a frequency spacing of $\Delta f_s = 0.416$ MHz, so that the time resolution is $\tau_{res} = \frac{1}{B_w} = 0.2$ ns and the maximum measurable excess delay is $\tau_{max} = 2400$ ns. The channel frequency response is measured using a PNA-E series microwave vector network analyzer (VNA) E8361A from Agilent. An intermediate frequency bandwidth of $B_{IF} = 50$ Hz is chosen to reduce the noise power within the measurement band, which improves the dynamic range. This is the receiver bandwidth for single sinusoid in the VNA; the smaller is IF bandwidth the larger the signal to noise ratio. Also each measurement is repeated 50 times to further average out the noise.

Due to the losses inside the VNA and 60 GHz coaxial cables, the measured signal at the receiver is weak. A 60 GHz solid state power amplifier (PA) from QuinStar Inc. (QGW-50662030-P1) was used to compensate for the losses and to improve the dynamic range. An illustration of the measurement set-up is provided in Fig. 2. As transmit and receive antennas, we used two identical open waveguide antennas for the 50-75 GHz frequency band, with aperture size 3.759×1.880 mm². The beam pattern of the antennas is shown in Fig. 3. The gain of the open waveguide antenna is

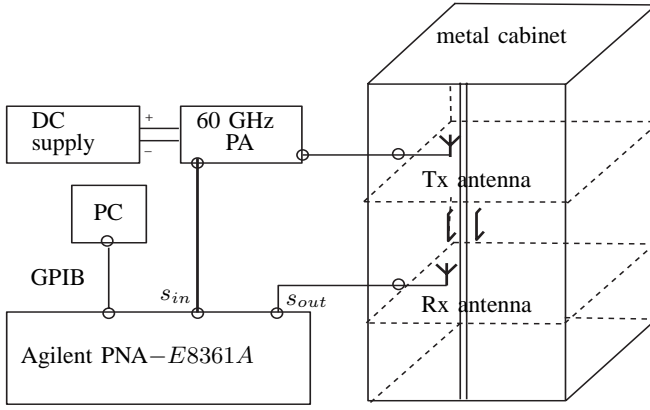


Fig. 2: Measurement setup for channel sounding inside the metal cabinet.

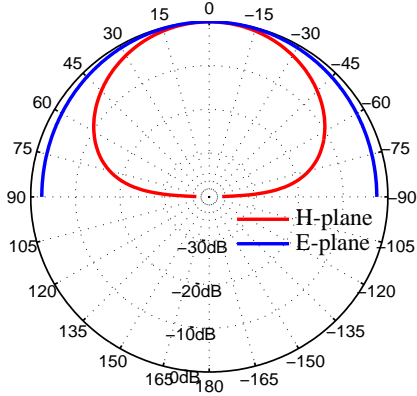


Fig. 3: Field radiated by the TE_{10} mode in open waveguide antenna with respect to θ angle.

about 4.6 dBi as calculated using [11]

$$G = \frac{4\pi A_e (f_c)^2}{c^2}, \quad (2)$$

where A_e is the effective aperture and c is the speed of light.

C. Measurement procedure

To investigate the channel behavior within the metal cabinet, we considered three scenarios.

Scenario 1 is a LOS scenario where we used a metal enclosure of dimension $100 \times 45 \times 45$ cm³. *Scenario 2* is a LOS scenario with a metal enclosure of a larger dimension, i.e., $100 \times 45 \times 180$ cm³. *Scenario 3* is an NLOS scenario with the same larger enclosure. Note that the volume of the metal enclosure in *scenario 2* and *scenario 3* is four times larger than the volume of the metal enclosure used for *scenario 1*. To block the LOS path, and create the NLOS scenario, a 50×45 cm metal separation plate is used in *scenario 3*.

The transmit and receive antennas were placed on a styrofoam (polystyrene) sheet, which acts as vacuum for radio waves and has a negligible effect on the channel behavior. The transmit and receive antennas were supported using metal clamps. The co-axial cables were drawn into the metal cabinet

	x -axis	y -axis	z -axis
Scenario 1	15-85 cm; 8 steps	5-30 cm; 6 steps	15, 30 cm
Scenario 2	15-85 cm; 8 steps	5-30 cm; 6 steps	35, 140 cm
Scenario 3	15-40 cm; 6 steps	5-30 cm; 6 steps	35, 140 cm

TABLE I: Receive antenna co-ordinates.

by means of small holes which are just sufficiently large to pass the cable.

For all scenarios, the location of the transmit antenna was kept fixed. The channel was measured at various locations in 3 dimensions, i.e., x, y, z axes, as specified in Table I. This produced 96, 96 and 72 receiver locations for scenario 1, 2 and 3, respectively.

In *scenario 1* and *scenario 2* the transmit antenna was fixed at co-ordinate $(x_t, y_t, z_t) = (65, 15, 0)$ cm, and in *scenario 3*, for the NLOS case the transmit antenna was located at $(x_t, y_t, z_t) = (15, 15, 0)$ cm.

III. DATA PROCESSING

A. Inverse filtering technique

Post-processing of the data is required to extract the channel impulse response (CIR) from the measured frequency domain signals. Prior to the IFFT, we cancel the antenna and instrument responses using an inverse filtering technique [12], [13], briefly explained as follows.

Let $x(t)$ be the transmitted signal, which is impaired by the measurement system and the antennas. The received signal $r(t)$ is modeled as

$$r(t) = x(t) * h_{tx}(t) * h_{sys}(t) * h(t) * h_{rx}(t), \quad (3)$$

where $h_{tx}(t)$ and $h_{rx}(t)$ are the impulse responses of the transmit and receive antennas, $h_{sys}(t)$ is the transfer function of the measurement system and $h(t)$ is the CIR of interest.

The CIR for free space without reflections or obstructions consists of a single LOS path, parametrized by an attenuation and a simple delay equal to the time-of-flight of the signal between the transmit and receive antenna. We can make a recording of the received signal at a known reference distance in free space, and after time gating obtain a reference signal $r_{fl}(t)$, modeled as

$$r_{fl}(t) \approx x(t) * h_{tx}(t) * h_{sys}(t) * h_{rx}(t), \quad (4)$$

so that

$$r(t) \approx r_{fl}(t) * h(t). \quad (5)$$

More specifically, $r_{fl}(t)$ in (4) absorbs the effect of the antennas and the system (this is not entirely accurate as the directionality of the antennas is ignored). The CIR is obtained from (5) via inverse filtering. Equivalently, in frequency domain, we can obtain the CFR $H(f)$ by

$$H(f) = \frac{R(f)}{R_{fl}(f)}. \quad (6)$$

The CIR is then obtained by taking the (windowed) IFFT of $H(f)$ and correction for the delay and attenuation (normalization).

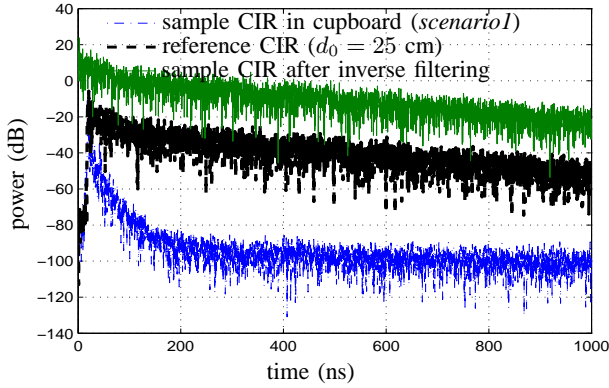


Fig. 4: Sample CIR from *scenario 1* before and after inverse filtering with Tx-Rx $d = 33$ cm apart, compared to the measured reference CIR (free space, Tx-Rx $d_0 = 25$ cm apart).

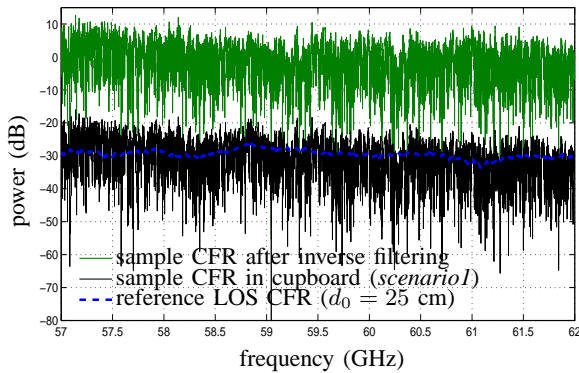


Fig. 5: Sample CFR from *scenario 1* before and after inverse filtering and reference CFR (free space).

We have obtained a reference LOS signal $r_{fl}(t)$ by placing the transmitter and receiver at a distance of 25 cm outside the metal cabinet (free space). The LOS path was retrieved by windowing the measured signal and truncating it after 50 ns (time gating), so as to remove noise and multipaths beyond the direct line of sight.

In Fig. 4, we show a sample measurement CIR within the metal cabinet (*scenario 1*, at 33 cm, with the transmitter and

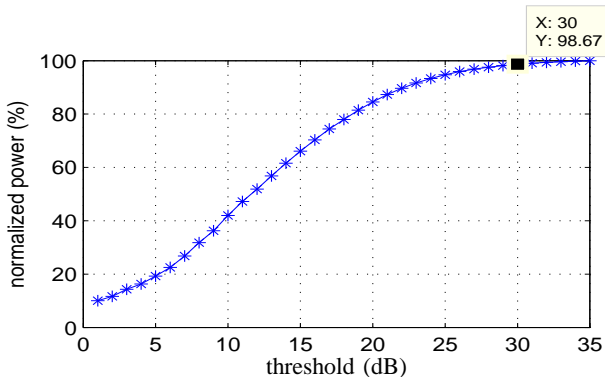


Fig. 6: Average received power for different thresholds in *scenario 1*.

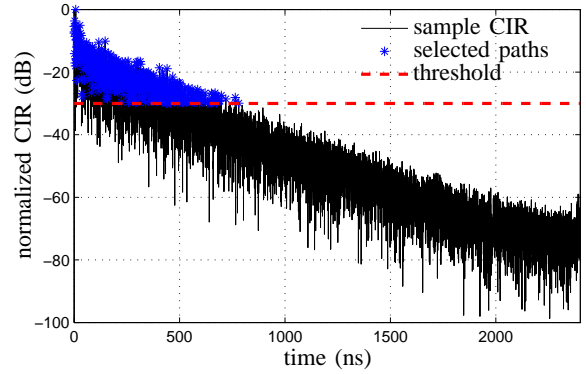


Fig. 7: Sample CIR with 30 dB threshold and received paths for *scenario 1*

receiver at different heights), as well as the measured free space signal. The figure illustrates the effect of the metal enclosure on the received multipaths which are above the noise floor even up to 1000 ns.

Fig. 5 shows the original frequency domain response (CFR) of the sample measurement from *scenario 1*, and the frequency domain signal $R_{fl}(f)$ of the truncated reference measurement $r_{fl}(t)$. The effect of inverse filtering can be observed in the calibrated plot where the sample CFR is normalized by $R_{fl}(f)$.

B. Normalization and thresholding

For model parameters that do not depend on the absolute power (i.e., the small-scale channel model considered in Sec.V), we have normalized the received signal to have a maximum value at 0 dB. The dynamic range of the received signal is in the order of 70 dB, considering the noise level at -70 dB after normalization.

For estimating statistics for individual path parameters, it is useful to truncate the duration of the channel. We apply a threshold level taking into account the noise level, the amount of total received power and the relevant multipath components [14], [15].

From Fig. 6 it can be observed that by setting a threshold at 30 dB below the strongest path, more than 98% of the total power is captured in *scenario 1*. This threshold is still well above the noise level. As an illustration, Fig. 7 shows a normalized received CIR with a threshold at -30 dB. The duration of this channel is still about 800 ns.

IV. LARGE-SCALE CHANNEL MODEL: PATH-LOSS

The large-scale channel model, specifically the path-loss model, is essential for any wireless system design to calculate its link budget. For a conventional channel (outdoor or indoor), the path-loss model suggests that the average received power decreases exponentially with increasing distance between transmitter and receiver. This is generally expressed in logarithmic scale as

$$P_L(d)_{dB} = P_L(d_0)_{dB} + \alpha 10 \log_{10}\left(\frac{d}{d_0}\right) + X_\sigma. \quad (7)$$

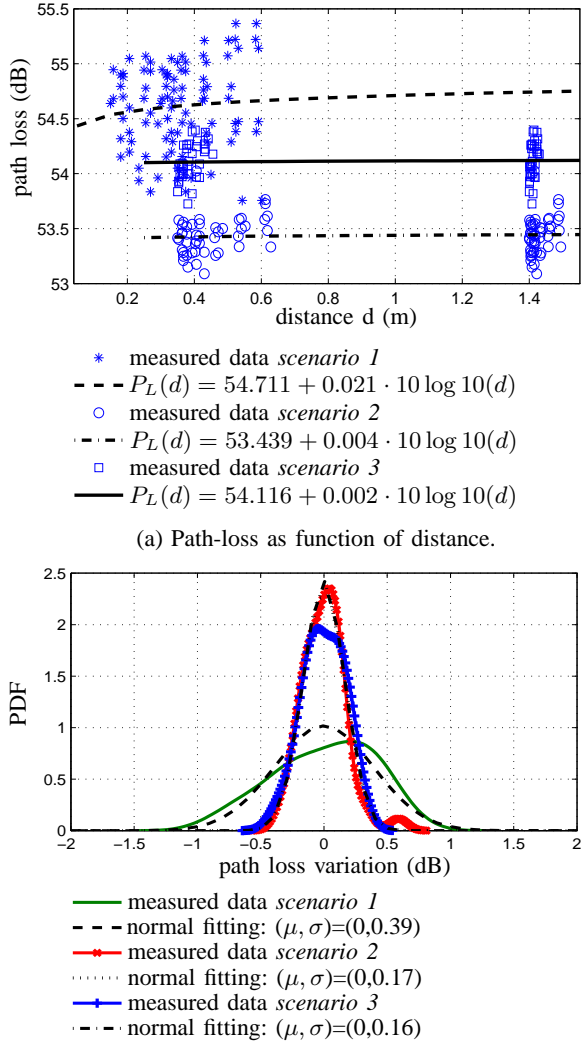


Fig. 8: Path-loss model parameter estimation.

where $P_L(d)_{dB}$ is the average received power at a distance d (m) relative to a reference distance d_0 (m), α represents the path-loss exponent, and X_σ is a zero-mean Gaussian random variable with standard deviation σ reflecting the attenuation (in dB) caused by flat fading (shadowing or slow fading).

Using the measurements of the received power for different distances between the transmit and receive antennas, we can estimate the path-loss exponent α . Accordingly, for each measurement the distance related path loss term ($P_t - P_r$) is calculated as shown in Fig. 8a which shows that the path-loss exponent α is very small (around 0.02-0.002), suggesting that in such a closed metal environment there is nearly no loss in the received power as function of distance. In comparison, for narrowband indoor systems some measurements have reported a path-loss exponent of α in the range 1.6 – 6 [16], and NLOS wireless personal area network (WPAN) measurements resulted in α in the range 0.04 – 0.09 [17], [14]. According to the Friis formula, the path-loss exponent for conventional indoor environments should be larger for transmissions at

60 GHz compared to lower carrier frequencies.

The ideal metal enclosed environment acts as a semi-conservative physical system where the only sources of absorptions are the antennas. The waves keep bouncing back and forth, and when the distance between the antennas is incremented the received power does not fluctuate because most of the energy reaches the receive antenna either directly or as multipath reflection in the metal cabinet.

Fig. 8b shows the probability density function (PDF) of X_σ , i.e., the fluctuation of the path-loss around the regression line in Fig. 8a. It is seen that the PDF approximately follows a normal distribution, with a standard deviation of 0.16–6 dB. Among the considered scenarios, the NLOS case (*scenario 3*) shows the smallest variation, and this is due to the larger distances (volume) and the obstructed LOS path.

V. SMALL-SCALE CHANNEL MODEL

The path-loss model describes the channel behavior in large-scale in terms of the attenuation as function of distance. The channel can be further characterized by its small-scale properties caused by reflections in the environment, which are modeled as multipath components. The n th multipath component is described by a power a_n^2 and arrival time t_n . Multipath leads to small-scale fading (variations over short distances due to constructive and destructive additions). The most important model parameters that describe small-scale variations are the RMS delay spread, the time decay constant, and the PDF of the multipath arrival times.

A. RMS delay spread (RDS)

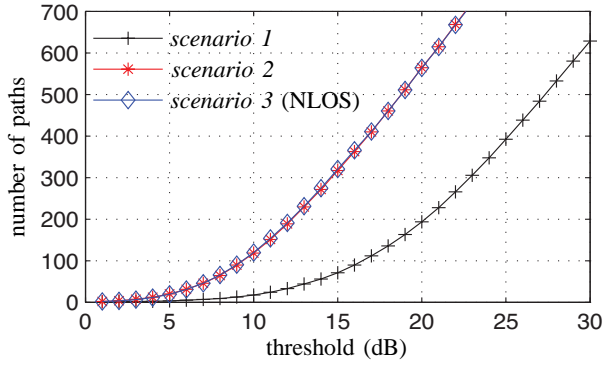
Delay spread describes the time dispersion effect of the channel, i.e., the distribution of the received power in time. A large delay spread causes severe intersymbol interference (ISI) and can deteriorate the system performance. The RMS delay spread (RDS) is a commonly used parameter to characterize this effect [18]. The RDS is obtained by first estimating the individual path parameters $\{(a_n^2, t_n)\}$ for each observation, and then computing

$$t_{rms} = \sqrt{\bar{t}^2 - (\bar{t})^2}, \quad \bar{t}^\beta = \frac{\sum_{n=1}^N a_n^2 t_n^\beta}{\sum_{n=1}^N a_n^2},$$

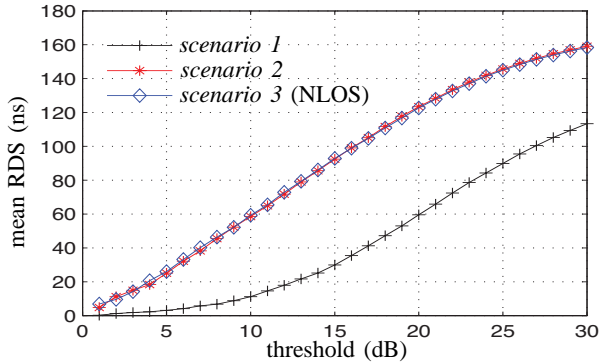
where \bar{t} , \bar{t}^2 and \bar{t}^β are the first, second and β moment of the power delay profile, respectively.

Fig. 9a shows the number of received paths for different power thresholds. As expected, the number of received paths (N) increases with increasing threshold level. In the same way, the RDS increases as the number of collected paths increases (Fig. 9b). At a threshold of 30 dB, the curves saturate and we used the corresponding value as the estimated RDS.

Fig. 10 shows the cumulative distribution function (CDF) of the estimated RDS values for each scenario. The figure also shows the fit to a normal distribution. The mean values of the normal distribution, obtained after fitting, reveals the average length of the channel. We obtained values of 113.4 ns (*scenario 1*), 159.1 ns (*scenario 2*) and 158.3 ns (*scenario 3*). These mean RDS values are significantly larger than conventional indoor channels, which are typically between



(a) Number of received paths



(b) mean RDS

Fig. 9: Number of received paths and RDS for different thresholds.

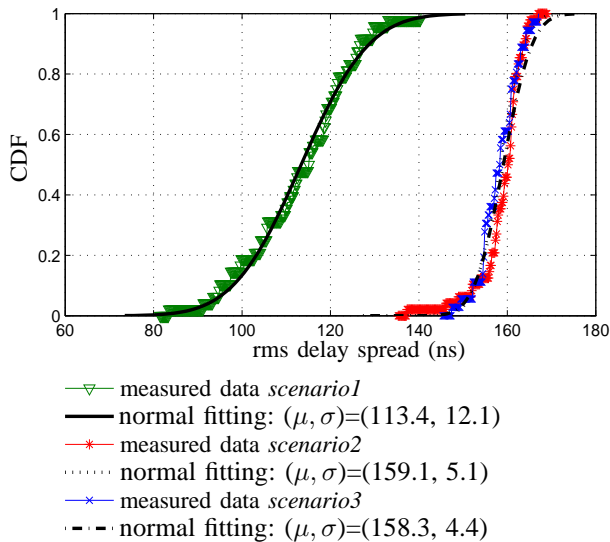


Fig. 10: Cumulative distribution function of RDS.

4–21 ns. These large values will impact the signal processing and system design within such environments, e.g., the channel equalization and residual inter block interference (IBI) after equalization, and hence, the achievable data rates.

Note that the estimated mean RDS is almost the same for *scenario 2* and *scenario 3*, which shows that there is a clear relation between the volume of such metal enclosures and RDS, independent of LOS and NLOS cases.

B. Time decay constant

Most current IEEE standard channel models are based on the Saleh-Valenzuela (SV) model [19], [20]. In this model, the multipaths are considered as a number of rays arriving within different clusters, and separate power decay constants are defined for the rays and the clusters.

Our measurement results do not show that the multipath components form clusters. A physical justification comes from the fact that multipath reflections are coming from the (same) walls. In this case, the average power delay profile (PDP) is defined by only one decay parameter γ rather than the common SV model with two decay parameters. The corresponding model is given by

$$\bar{a}_n^2 = \bar{a}_0^2 \exp(-t_n/\gamma), \quad (8)$$

where \bar{a}_0^2 and \bar{a}_n^2 are the (statistical) average power of the first and n th multipath component, respectively, and γ is the power decay time constant for arriving rays, assumed as a random variable. We estimate a γ_k for each measurement in every scenario using a least-squares curve fitting on $\log(a_n^2)/\log(a_0^2)$, as shown by the examples in Fig. 11.

Based on these estimates for the γ_k s, the PDF for γ is plotted and fitted to Gaussian, Gamma, and Weibull distributions for each considered scenarios, as shown in Fig. 12. These distributions are commonly used to statistically model γ [17], [14]. We use the Gaussian mean as γ for the rest of paper. The Gamma distribution is given by

$$f(x|\alpha, \beta) = \frac{x^{\alpha-1}}{\beta^\alpha G(\alpha)} \exp(-\frac{x}{\beta}), \quad (9)$$

where $G(\alpha)$ is a Gamma function, and the parameters α and β are computed for all scenarios from the empirical data. The Weibull distribution is expressed as

$$f(x|\zeta, k) = \begin{cases} \frac{k}{\zeta^k} x^{k-1} \exp(-(\frac{x}{\zeta})^k) & \text{if } x \geq 0 \\ 0 & \text{if } x < 0 \end{cases} \quad (10)$$

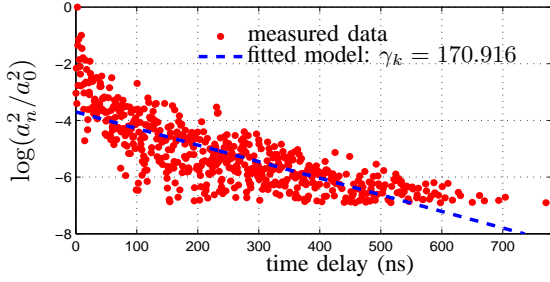
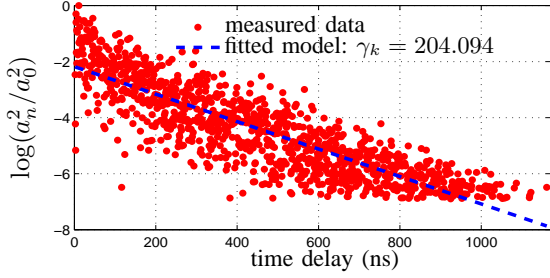
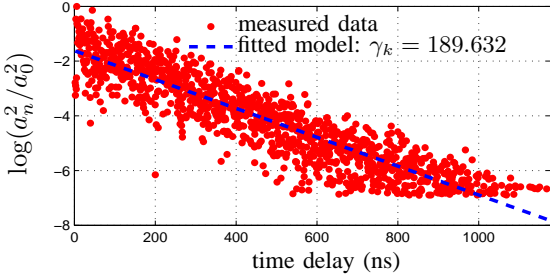
where the scale and shape parameters are ζ and k respectively.

C. Multipath arrival times

Without considering clusters, the multipath arrival times t_n would typically for indoor channels [17] be modeled as a single Poisson process. Accordingly, the inter-arrival times $t_n - t_{n-1}$ are modeled by an exponential PDF as

$$p(t_n|t_{n-1}) = \lambda \exp(-\lambda(t_n - t_{n-1})) \quad (11)$$

where λ is the mean arrival rate of the multipath components. It is motivated in [14] that when the measured arrival times deviate too much from the single Poisson model, a mixture

(a) sample measurement in *Scenario 1*(b) sample measurement in *Scenario 2*(c) sample measurement in *Scenario 3*Fig. 11: LS fit for time decay constant is leading to an estimated γ_k for each measurement.

of two Poisson processes is more suitable for modeling their arrival times. The mixture of two Poisson processes can be expressed as

$$p(t_n|t_{n-1}) = b \lambda_1 \exp(-\lambda_1(t_n - t_{n-1})) + (1 - b) \lambda_2 \exp(-\lambda_2(t_n - t_{n-1})) \quad (12)$$

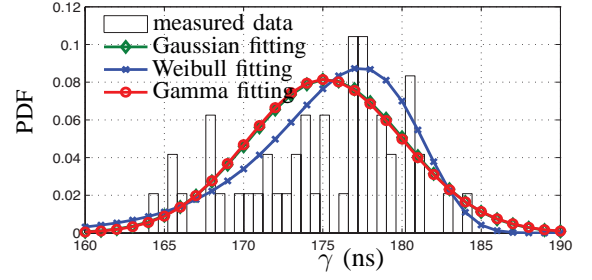
where λ_1 and λ_2 are the arrival rates and parameter $0 \leq b \leq 1$ is the mixing probability.

Fig. 13 shows the corresponding estimated parameters. As seen, the mixed Poisson process provides a much closer fit to the measured data than the conventional single Poisson process. Apparently, if the RDS or channel length is large, the arriving paths appear over a wide range of time differences which makes it difficult to be represented by only one Poisson parameter.

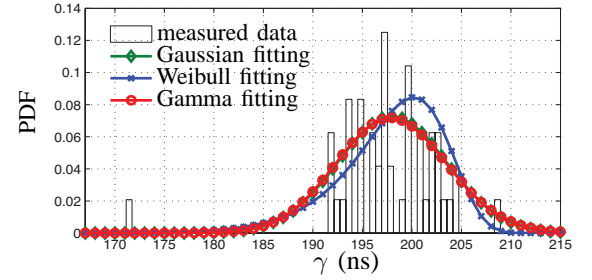
VI. COMPARISON TO 802.15 CHANNEL MODELS

The estimated parameters for the channel model are summarized in Table III. In this table, the listed parameters are:

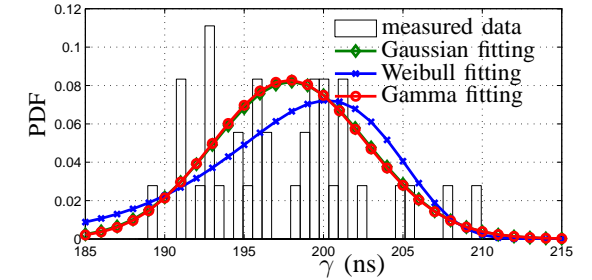
- $P_L(d_0)$: path-loss at reference distance d_0 (m)
- α : path-loss exponent
- σ_{P_L} : path-loss log-normal standard deviation

(a) *Scenario 1*

$$\begin{aligned} \text{Gaussian}(\mu, \sigma) &= (175.2, 4.901) \\ \text{Gamma}(\alpha, \beta) &= (1281, 0.137) \\ \text{Weibull}(\zeta, k) &= (177.5, 42.28) \end{aligned}$$

(b) *Scenario 2*

$$\begin{aligned} \text{Gaussian}(\mu, \sigma) &= (197.9, 5.481) \\ \text{Gamma}(\alpha, \beta) &= (1265, 0.156) \\ \text{Weibull}(\zeta, k) &= (200.3, 46.05) \end{aligned}$$

(c) *Scenario 3*

$$\begin{aligned} \text{Gaussian}(\mu, \sigma) &= (197.9, 4.865) \\ \text{Gamma}(\alpha, \beta) &= (1689, 0.117) \\ \text{Weibull}(\zeta, k) &= (200.4, 39.37) \end{aligned}$$

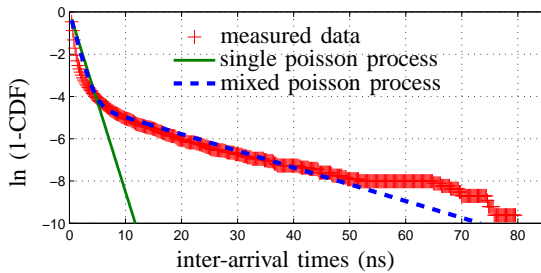
Fig. 12: PDF fittings for time decay constant γ .

- \bar{L} : mean RMS delay spread (RDS)
- Λ : cluster arrival rate
- λ : ray arrival rate (single Poisson fit)
- Γ : power decay constant for clusters
- γ : power decay constant for rays
- σ_Γ : cluster power decay log-normal standard deviation
- σ_γ : ray power decay log-normal standard deviation

Also, the corresponding parameters of the standard IEEE 802.15 channel model are shown. The numbers are taken from [21], which provides models for wideband (9 GHz bandwidth) channels at 60 GHz carrier frequency. The reported parameters are selected from the CM1, CM4, and CM9 channel models suggested in this document and obtained from the measurements in residential LOS environment, office area in NLOS scenario, and within a kiosk with LOS, respectively.

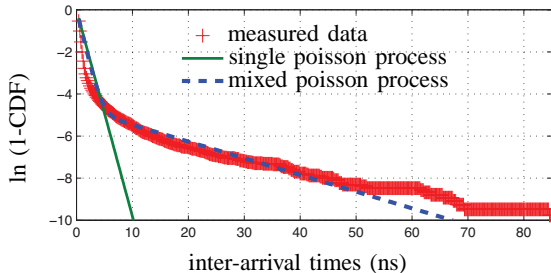
Parameter	Unit	Metal cabinet			IEEE 802.15		
		Sc. 1	Sc.2	Sc. 3	CM1	CM4	CM9
		LOS	LOS	NLOS	LOS	NLOS	LOS
$P_L(d_0)$	dB	54.711	53.439	54.116	75.1	56.1	NA
α		0.02	0.004	0.002	1.53	3.74	NA
σ_{PL}	dB	0.39	0.17	0.16	1.5	8.6	NA
\bar{L}	ns	113.4	158.3	159.1	NA	NA	NA
Λ	1/ns	-	-	-	0.144	0.07	0.044
λ	1/ns	0.985	1.037	1.094	1.17	1.88	1.01
Γ	ns	-	-	-	21.5	19.44	64.2
γ	ns	175.23	197.99	197.93	4.35	0.42	61.1
σ_Γ	ns	-	-	-	3.71	1.82	2.66
σ_γ	ns	4.90	5.48	4.86	7.31	1.88	4.39

TABLE II: Comparison of various channel parameters of the measured channels, compared to IEEE 802.15 channel models. Abbreviation “NA” stands for not available and “-” means not applicable here.



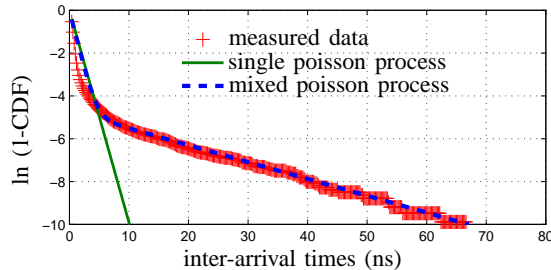
(a) Scenario 1:

$$\lambda = 0.985, (\lambda_1, \lambda_2, b) = (0.083, 1.180, 0.015).$$



(b) Scenario 2:

$$\lambda = 1.037, (\lambda_1, \lambda_2, b) = (0.059, 1.219, 0.008).$$



(c) Scenario 3:

$$\lambda = 1.094, (\lambda_1, \lambda_2, b) = (0.084, 1.235, 0.009).$$

Fig. 13: Logarithm of the complementary CDF of the inter-arrival times.

It can be seen from Table III that the measured channel in a metal enclosure differs significantly from the typical wireless channels that are used in the literature to design a wireless link for short range communications. The main distinctions are:

- 1) Very small path-loss exponent in both LOS and NLOS cases,
- 2) Significantly longer channels or equivalently very large RDS,
- 3) Arriving rays do not form clusters,
- 4) Arrival rate is modeled here as a mixed Poisson process.

Obviously, the very small path-loss exponent and resulting very large RDS are caused by the non-damping effect of the metal walls. The resulting long channels in metal enclosure environment make wireless system design and the involved signal processing both an interesting as well as a challenging task.

VII. SYSTEM DESIGN EXAMPLE

Channel models are generally used for system design. For the presented model of a metal enclosure at 60 GHz, a distinguishing feature is the very large delay spread. Correspondingly, the rich multipath makes the wireless channel very frequency selective, as is clear in Fig. 5. For such a channel, OFDM is an appropriate modulation scheme, and is indeed considered for most of the existing wideband wireless standards including WiMAX, LTE, WiFi, and also for the upcoming new standard for 60 GHz WPAN, i.e., IEEE 802.15.3c. In the usual designs, the frequency band is divided into several subcarriers such that each subcarrier experiences a flat-fading channel.

In this section, we compare the performance of an OFDM system using the measured channel to that using a simulated Rayleigh fading channel. This provides directions and questions for further work, such as

- What are suitable modulation schemes and equalization techniques for such dispersive (rich scattering) and extremely long channels?
- Can we benefit from the diversity gain offered by these types of channels with an acceptable computational com-

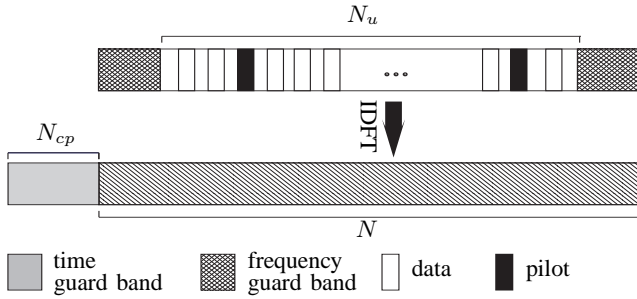


Fig. 14: data sequence with frequency guard bands (null subcarriers in frequency domain) and pilot subcarriers is converted to the time domain OFDM block by taking IDFT and appending the time domain guard (cyclic prefix) to the block.

plexity or should the channel be shortened using e.g. absorbers?

- What is the channel capacity for such highly reflective environments?

For the numerous existing wireless channel models, these questions are well studied. The initial approach would be to relate the proposed channel model to the available models and modify the system design including the modulation, coding and equalization in order to cope with the new circumstances.

A. Design parameters

The design example is based on a single antenna, standard OFDM modulation without coding (see Fig. 14). An OFDM block with bandwidth B_w is split into N subcarriers, consisting of guard bands and N_u 'user' subcarriers (data and pilots). In time domain, the corresponding N samples are augmented with a cyclic prefix of N_{cp} samples. The symbol duration is $T_s = 1/B_w$. Straightforward equalization requires that the time duration of the cyclic prefix is larger than the length of the wireless channel:

$$N_{cp}T_s > t_{max} \quad (13)$$

This is used to isolate the ISI within each block of the OFDM symbol so that the ISI can be eliminated separately in each block by frequency domain equalization.

We assume M -ary modulation, with $M = 2^l$, so that a symbol consists of l bits. The bandwidth efficiency is

$$\kappa = \frac{l N_u}{N_{cp} + N}$$

and the resulting data rate is κ/T_s bits per second. The data rate can be increased by increasing l but this will reduce the SNR and lead to a higher bit-error rate (BER). We can also increase N_u (hence also N) until the bandwidth efficiency saturates to l . Finally, the symbol duration T_s can be shortened by increasing the available bandwidth B_w .

Latency is often also a consideration, and this leads to a limitation of the size of a data packet. One OFDM block will have a duration of

$$(N_{cp} + N)T_s$$

and some systems pose a maximum to this.

Several other limitations are in place. Apart from practical limitations and computational limitations, the number of subcarriers (N) that can be allocated in one OFDM block is limited by the requirement that the channel is constant over the duration of the OFDM symbol, i.e., the coherence time of the channel should be larger. The coherence time is defined as $\frac{1}{\Delta f_D}$ where Δf_D is the range of possible Doppler frequencies of the channel, and the requirement becomes [18]

$$(N + N_{cp}) \Delta f_D T_s \ll 1, \quad (14)$$

Another requirement is that each subcarrier experiences flat fading. In frequency domain, the distance between fades is related to $1/t_{max}$. This leads to [18]

$$N \gg B_w t_{max} \quad (15)$$

As an example, let us design a system at $f_c = 60$ GHz with an available bandwidth $B_w = 5$ GHz. For the sake of simplicity, we consider BPSK modulation, which leads to $l = 1$ and $T_s = \frac{1}{B_w} = 0.2$ ns.

The proposed system is part of a mechatronic system in a closed metal environment in which a moving platform with sensors and actuators has to communicate to a controller in the "fixed" world. Since movements that occur outside the enclosure do not affect the channel, we expect a slowly time-varying channel with a sufficiently long coherence time. The Doppler shift is defined as $\Delta f_D = \frac{\nu f_c}{c}$, where ν is the relative speed between transmitter and receiver, c is the speed of light, and f_c is the carrier frequency. If we assume a maximum relative speed of 10 ms $^{-1}$, then the Doppler frequency range is $\Delta f_D = 2$ kHz, and the coherence time of the channel is $\frac{1}{\Delta f_D} = 0.5$ ms.

As discussed earlier, the spectral efficiency increases with the number of subcarriers. Considering (14) for $\Delta f_D T_s = 0.4 \cdot 10^{-6}$, the upper bound on the length of an OFDM block is given by $N_{cp} + N \ll 2.5 \cdot 10^6$. To satisfy this, we consider as constraint on the size of a transmission block

$$N_{cp} + N < 2.5 \cdot 10^5 \text{ symbols.}$$

The cyclic prefix N_{cp} should satisfy (13). For a channel of length $t_{max} = 1\mu\text{s}$, this leads to

$$N_{cp} \geq 5000.$$

The exact number depends on the scenario. Finally, condition (15) leads to

$$N \gg 5000.$$

We consider two versions of the system: (A) minimal latency; (B) maximal data rate. For minimal latency, we take $N_{cp} = 5000$, and a block size of $N = 2^{13} = 8192$ of which we take $N_u = 6720$ data/pilot symbols, and $2 \times N_{\text{guard}} = 1472$ null subcarriers for frequency guards at both ends of a block. This leads to a spectral efficiency of $\kappa \approx 0.5$. The duration of one data packet becomes $2.64 \mu\text{s}$ and the data rate is 2.547 Gbps.

For maximal data rate, we choose $N = 2^{17} \approx 1.3 \cdot 10^5$, of which we take $N_u = 107520$ data/pilot symbols, and $2 \times N_{\text{guard}} = 23552$ null subcarriers. The duration of one data packet is about $27.2 \mu\text{s}$ and the data rate is 3.95 Gbps. Thus, latency increases almost 10 times by taking $N = 2^{17}$

compared to $N = 2^{13}$ where as the data rate increases by less than 50%.

For the measured channels, the channel length t_{max} varies depending on the scenario, which alters the cyclic prefix and consequently the block length. Table III summarizes the parameters that are used in the simulation. As usual, higher data rates could be obtained by considering higher-level modulation as well as multiple antennas.

B. Simulation setup

For the designed BPSK-OFDM systems, we will compare the BER performance for both simulated Rayleigh fading channels and the measured channels for the various scenarios. The Rayleigh fading channel is based on a tapped delay line setup where each path is assumed to be a Rayleigh fading process without considering any specific power delay profile.

The considered performance measure is BER as function of E_b/N_0 , where E_b is the transmit energy per bit, and $\frac{N_0}{2}$ is the two-sided noise power spectral density (PSD). In the simulation, we first convert E_b to the energy per symbol E_s , taking into account the number of bits per symbol l and the overhead by the cyclic prefix N_{cp} , resulting in

$$\frac{E_s}{N_0} = \frac{E_b}{N_0} \cdot \frac{lN_u}{N_{cp} + N}. \quad (16)$$

The measured and simulated channels are normalized to unit power and convolved with the transmit sequence. In that case, the transmitted E_s/N_0 is equal to the received signal to noise ratio (SNR), and we add white Gaussian noise of suitable power to obtain the specified SNR.

For such dispersive channels, several subcarriers experience fading so that the BER is usually not very good. Various well-known techniques could be introduced to combat the fading subchannels, e.g., channel coding, interleaving, rake receiver design, as well as single input multiple output (SIMO) systems with diversity combining schemes [18]. However, for improved interpretation of the results, we will not consider these in the simulation.

In the simulation, we assume that the receiver has perfect knowledge of the channel.

C. Simulation results

Fig. 15 shows the BER as a function of E_b/N_0 for the various channels. As expected, the performance is generally limited by the fading channel as the symbols in channel nulls cannot be recovered by frequency domain equalization. For the larger block size (design (B)), the BER performance is slightly (almost 3 dB) better than the shorter OFDM block, as expected, due to the spectral efficiency and less spread of transmit power over the cyclic symbols.

VIII. SUMMARY AND CONCLUDING REMARKS

In this paper, a comprehensive channel model is provided for 60 GHz transmission inside a metal enclosure based on channel measurement results for different scenarios including the LOS and NLOS situations. Significantly long channels together with very rich multipath reflected from the metal walls

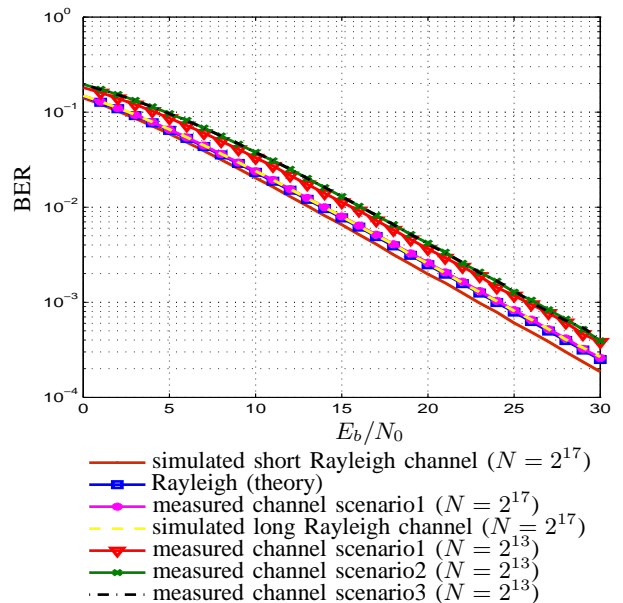


Fig. 15: BER performance of an uncoded OFDM system over the measured channels for different scenarios with block size $N = 8192$ and $N = 2^{17}$. The BER plot of OFDM block of size $N = 2^{17}$ is shown for *scenario1*, (*scenario2* and *3* have the same BER curves as *scenario1*), and also for two simulated Rayleigh fading channels with $L = 10$ and $L = 4000$ taps. A theoretical BER curve for a narrowband signal (No ISI) is plotted as a reference.

are the most distinguishing features of such channels. Both large-scale and small-scale channel characteristic parameters are compared with other 60 GHz modeling results for short range wireless communication which indicates a noticeable difference between transmission in a metal surrounding and conventional indoor environments.

An uncoded OFDM system design example is elaborated, and the BER performance is studied using the measured channels, which identifies the fading effect on the system functionality. We considered OFDM because time domain equalization is computationally expensive for such long channels. Moreover, to combat the poor BER due to frequency-domain fades, some form of coding should be used, which further reduces the bandwidth efficiency. To limit the loss of data rate due to the long cyclic prefix, channel shortening or per-tone equalization techniques [22], [23] could be used.

The system design example shows that high data rates and reasonable latencies are feasible, thus enabling interesting applications in demanding mechatronic systems. The computational complexity will have to be verified. Further data rate improvements are possible by exploiting the rich scattering environment in combination with large MIMO antenna arrays (that will be compact at 60 GHz), which will also boost the SNR due to improved spatial diversity. The latency of the system is determined by the long channel impulse response and the long cyclic prefix. If latency is an issue, physical remedies can be suggested including an absorbing coating inside the metal enclosure [24], if restrictions on installing

	N_{cp}	A: $N = 2^{13}$		B: $N = 2^{17}$	
		bit-rate (Gbps)	Latency (μs)	bit-rate (Gbps)	Latency (μs)
Simulated 1	11	4.096	1.640	4.101	26.216
Simulated 2	4001	2.756	2.438	3.980	27.015
Scenario 1	3903	2.778	2.418	3.983	26.994
Scenario 2	5812	2.399	2.801	3.927	27.377
Scenario 3	5617	2.433	2.762	3.933	27.338

TABLE III: Data rates and latency for (A) a low-latency system, and (B) a high-rate system.

such bulky materials inside the mechatronic system permits this.

ACKNOWLEDGMENT

We would like to thank Dr. Marco Spirito and the staff of the Electronics Research Laboratory at TU Delft for providing the channel measurement setup.

REFERENCES

- [1] R. Daniels, J. Murdock, T. Rappaport, and R. Heath, "60 GHz wireless: Up close and personal," *IEEE Microw. Mag.*, vol. 11, no. 7, pp. 44–50, Dec. 2010.
- [2] R. Daniels and R. Heath, "60 GHz wireless communications: emerging requirements and design recommendations," *IEEE Veh. Technol. Mag.*, vol. 2, no. 3, pp. 41–50, Sept. 2007.
- [3] "IEEE standard for high rate wireless personal area networks (WPANs): Millimeter-wave-based alternative physical layer extension," *IEEE Std 802.15.3c-2009 (Amendment to IEEE Std 802.15.3-2003)*, pp. c1–187, Dec. 2009.
- [4] P. F. M. Smulders, "Statistical characterization of 60 GHz indoor radio channels," *IEEE Trans. Antennas Propag.*, vol. 57, no. 10, pp. 2820–2829, 2009.
- [5] H. Xu, V. Kukshya, and T. Rappaport, "Spatial and temporal characteristics of 60-GHz indoor channels," *IEEE J. Sel. Areas Commun.*, vol. 20, no. 3, pp. 620–630, 2002.
- [6] N. Moraitis and P. Constantinou, "Measurements and characterization of wideband indoor radio channel at 60 GHz," *IEEE Trans. Wireless Commun.*, vol. 5, no. 4, pp. 880–889, 2006.
- [7] K. O. Kim, B. Floyd, J. Mehta, H. Yoon, C.-M. Hung, D. Bravo, T. Dickson, X. Guo, R. Li, N. Trichy, J. Caserta, I. Bomstad, W.R., J. Branch, D.-J. Yang, J. Bohorquez, E. Seok, L. Gao, A. Sugavanam, J. J. Lin, J. Chen, and J. Brewer, "On-chip antennas in silicon ICs and their application," *IEEE Trans. Electron Devices*, vol. 52, no. 7, pp. 1312–1323, 2005.
- [8] F. Rusek, D. Persson, B. K. Lau, E. Larsson, T. Marzetta, O. Edfors, and F. Tufvesson, "Scaling up MIMO: Opportunities and challenges with very large arrays," *IEEE Signal Process. Mag.*, vol. 30, no. 1, pp. 40–60, Jan. 2013.
- [9] S. Khademi, S. P. Chepuri, G. Leus, and A.-J. van der Veen, "Zero-forcing pre-equalization with transmit antenna selection in MIMO systems," in *Proc. of ICASSP*, 2013.
- [10] J. Parsons, D. Demery, and A. Turkmani, "Sounding techniques for wideband mobile radio channels: a review," *Proc. of IPCSV*, vol. 138, no. 5, pp. 437–446, Oct. 1991.
- [11] C. A. Balanis, *Antenna theory: analysis and design*. J. Wiley, New York, 1982.
- [12] A. Siamarou and M. Al-Nuaimi, "A wideband frequency-domain channel-sounding system and delay-spread measurements at the license-free 57 to 64 GHz band," *IEEE Trans. Instrum. Meas.*, vol. 59, no. 3, pp. 519–526, 2010.
- [13] S. Ghassemzadeh, R. Jana, C. Rice, W. Turin, and V. Tarokh, "Measurement and modeling of an ultra-wide bandwidth indoor channel," *IEEE Trans. Commun.*, vol. 52, no. 10, pp. 1786–1796, 2004.
- [14] Z. Irahauten, H. Nikookar, and G. J. M. Janssen, "An overview of ultra wide band indoor channel measurements and modeling," *IEEE Microw. Wireless Compon. Lett.*, vol. 14, no. 8, pp. 386–388, Aug. 2004.
- [15] Z. Irahauten, A. Yarovoy, G. J. M. Janssen, H. Nikookar, and L. Ligthart, "Suppression of noise and narrowband interference in uwb indoor channel measurements," in *Proc. of ICU*, 2005, pp. 108–112.
- [16] T. S. Rappaport, *Wireless Communications: Principles and Practice*. Prentice Hall, 1996.
- [17] Z. Irahauten, A. Yarovoy, G. Janssen, H. Nikookar, and L. Ligthart, "Ultra-wideband indoor propagation channel: Measurements, analysis and modeling," in *Proc. of EuCAP*, Nov. 2006, pp. 1–6.
- [18] A. Goldsmith and A. Nin, "Wireless communications," 2005.
- [19] A. Saleh and R. Valenzuela, "A statistical model for indoor multipath propagation," *IEEE J. Sel. Areas Commun.*, vol. 5, no. 2, pp. 128–137, Jan. 1987.
- [20] Q. Spencer, M. Rice, B. Jeffs, and M. Jensen, "A statistical model for angle of arrival in indoor multipath propagation," in *Proc. of VTC*, vol. 3, 1997, pp. 1415–1419.
- [21] "Task group 3c (TG3c) channel modeling sub-committee final report," IEEE P802.15 working group for wireless personal area networks (WPANs), Tech. Rep., Mar. 2007.
- [22] G. Leus and M. Moonen, "Per-tone equalization for MIMO OFDM systems," *IEEE Trans. Signal Process.*, vol. 51, no. 11, pp. 2965–2975, 2003.
- [23] I. Barhumi, G. Leus, and M. Moonen, "Time-domain and frequency-domain per-tone equalization for OFDM over doubly selective channels," vol. 84, no. 11, 2004, pp. 2055–2066.
- [24] O. Hashimoto, T. Abe, Y. Hashimoto, T. Tanaka, and K. Ishino, "Realisation of resistive-sheet type wave absorber in 60 GHz frequency band," *Electronics Letters*, vol. 30, no. 8, pp. 657–658, 1994.